TECTONICS, VOL. 32, 1176–1189, doi:10.1002/tect.20071, 2013

Dating brittle tectonic movements with cleft monazite: Fluid-rock interaction and formation of REE minerals

A. Berger,[1,2] E. Gnos,[3] E. Janots,[4] M. Whitehouse,[5] M. Soom,[6] R. Frei,[2] and T. E. Waight[2]

Received 1 May 2013; revised 12 July 2013; accepted 1 August 2013; published 1 October 2013.

[1] Two millimeter-sized hydrothermal monazites from an open fissure (cleft) that developed late during a dextral transpressional deformation event in the Aar Massif, Switzerland, have been investigated using electron microprobe and ion probe. The monazites are characterized by high Th/U ratios typical of other hydrothermal monazites. Deformation events in the area have been subdivided into three phases: (D_1) main thrusting including formation of a new schistosity, (D_2) dextral transpression, and (D_3) local crenulation including development of a new schistosity. The two younger deformational structures are related to a subvertically oriented intermediate stress axis, which is characteristic for strike slip deformation. The inferred stress environment is consistent with observed kinematics and the opening of such clefts. Therefore, the investigated monazite-bearing cleft formed at the end of D_2 and/or D_3, and during dextral movements along NNW dipping planes. Interaction of cleft-filling hydrothermal fluid with wall rock results in rare earth element (REE) mineral formation and alteration of the wall rock. The main newly formed REE minerals are Y-Si, Y-Nb-Ti minerals, and monazite. Despite these mineralogical changes, the bulk chemistry of the system remains constant and thus these mineralogical changes require redistribution of elements via a fluid over short distances (centimeter). Low-grade alteration enables local redistribution of REE, related to the stability of the accessory phases. This allows high precision isotope dating of cleft monazite. $^{232}Th/^{208}Pb$ ages are not affected by excess Pb and yield growth domain ages between 8.03 ± 0.22 and 6.25 ± 0.60 Ma. Monazite crystallization in brittle structures is coeval or younger than 8 Ma zircon fission track data and hence occurred below 280°C.

Citation: Berger, A., E. Gnos, E. Janots, M. Whitehouse, M. Soom, R. Frei, and T. E. Waight (2013), Dating brittle tectonic movements with cleft monazite: Fluid-rock interaction and formation of REE minerals, *Tectonics*, *32*, 1176–1189, doi:10.1002/tect.20071.

1. Introduction

[2] "Alpine" clefts are tectonically formed centimeter- to meter-sized, oriented voids in fissures and veins that become filled with hydrothermal fluid from which different minerals crystallize repetitively on the cleft walls. Formation of cleft is related to the prevailing tectonic stress field. Cleft mineralization has been systematically studied in the Alps by conventional stable isotope and/or fluid inclusion techniques [e.g., *Poty et al.*, 1974; *Mullis et al.*, 1994; *Sharp et al.*, 2005; *Tarantola et al.*, 2007]. These data show that the fluid pockets behave like a closed system and that they interact and equilibrate with the surrounding rock wall. Each deformation of the cleft is followed by an equilibration stage. Recently, U-Th-Pb systematics of cleft monazite have been found to be a powerful tool to provide new insights into cleft fluid evolution in combination with ages of mineral crystallization [*Janots et al.*, 2012]. The fluid composition in the cleft controls chemical redistribution of elements and influences the mechanical properties of the host rock. Constraining the timing of cleft formation by isotope dating provides further insights into the tectonic evolution at very low-grade metamorphic conditions, where brittle deformational regimes dominate. The time-deformation data that can be obtained from cleft mineralization can be compared with mica cooling ages and fission track data obtained on surrounding rocks. A major advantage of the method is that cleft monazite isotope dating provides precise ages. This is a result of essentially negligible issues with diffusion in the Th/Pb system at very low-grade conditions and the structural control between the cleft (brittle structure) and the mineralization. The precise monazite ages can be compared with geothermochronometers, which are based on temperature-controlled processes such as diffusion or annealing in a lattice (fission track dating). The comparison of Th/Pb low temperature crystallization ages with other thermochronometers provides further insights in exhumation history and timing of brittle structures.

Additional supporting information may be found in the online version of this article.

[1]Institute of Geological Sciences, University of Bern, Bern, Switzerland.
[2]Department of Geosciences and Natural Resource Management (Geology Section), Copenhagen University, Copenhagen, Denmark.
[3]Natural History Museum, Geneva, Switzerland.
[4]ISTerre, Grenoble, France.
[5]Laboratory for Isotope Geology, Swedish Museum of Natural History, Stockholm, Sweden.
[6]Geotest, Zollikofen, Switzerland.

Corresponding author: A. Berger, Institute of Geological Sciences, University of Bern, Baltzerstrasse 1 + 3, CH-3012 Bern, Switzerland. (alfons.berger@geo.unibe.ch)

0278-7407/13/10.1002/tect.20071

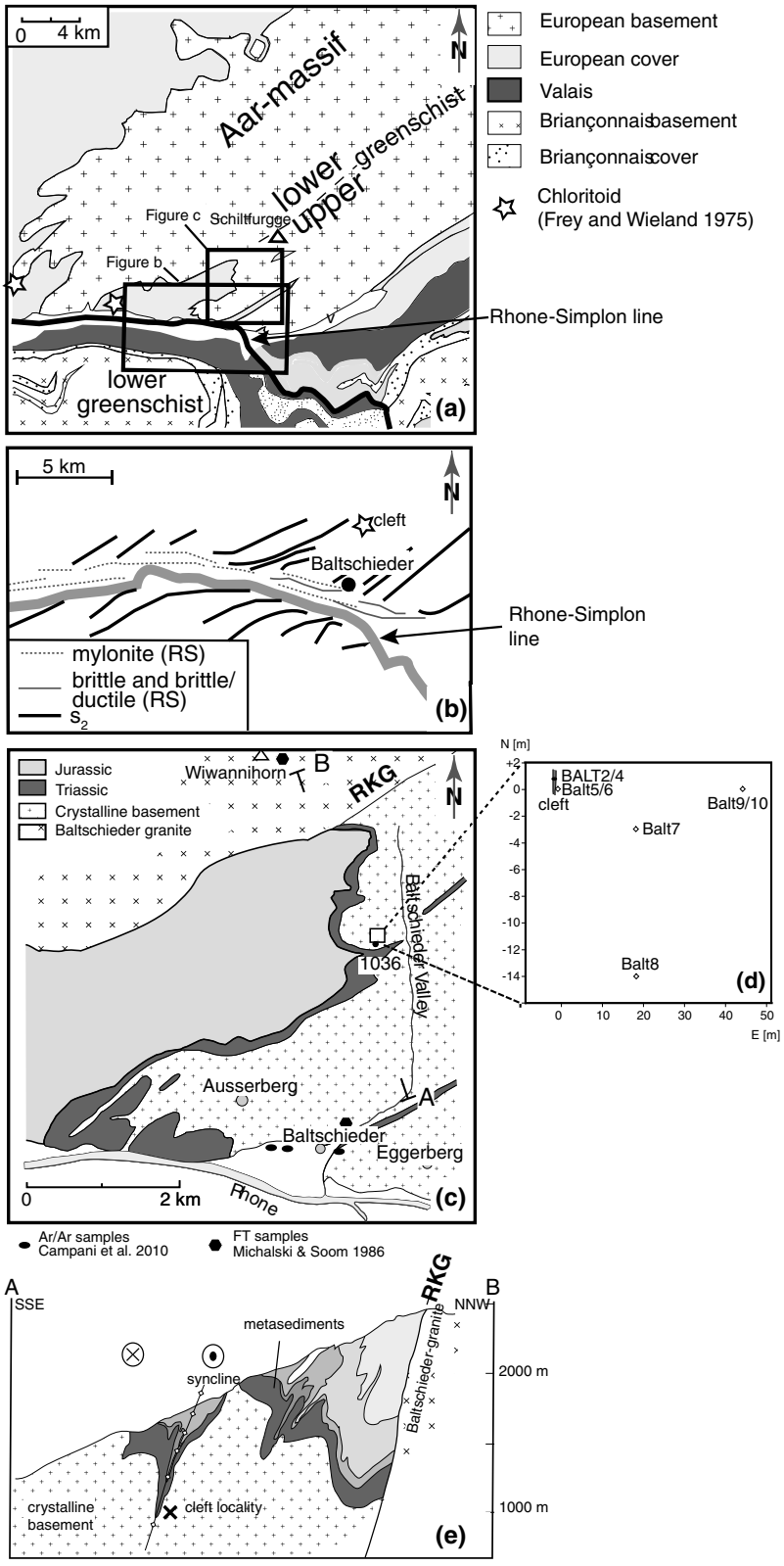

Figure 1. (a) Tectonic sketch map of the Valais area, Switzerland. The lower/upper greenschist boundary is from *Bousquet et al*. [2012]. (b) Planar structures following the Rhone valley, after *Campani et al*. [2010]. Note the orientation of the Rhone-Simplon fault rocks and the S_2 main foliation both indicating dextral shear. (c) Geological-tectonic sketch map of the area around Baltschieder valley, based on *Soom* [1986]; see Figure 1a for location. (d) Sample localities in and around the cleft relative to the cleft entrance. (e) Cross section of the study area in the Baltschieder valley (see Figure 1c for location) showing the position of the studied cleft. Data from *Dolivo* [1982]. Abbreviations: RS: Rhone-Simplon line; RKG: Rote-Kuh-Gampel fault.

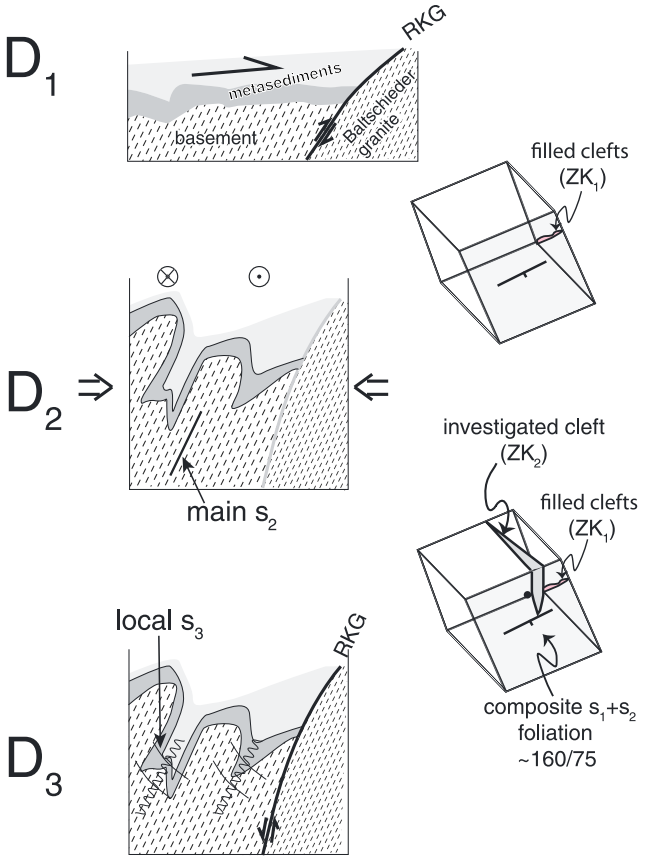

Figure 2. Sketches displaying the main Alpine deformation phases (D_1–D_3) of the study area and the formation of clefts in relation with the deformation phases. ZK: clefts; RKG: Rote-Kuh-Gampel fault.

[3] Cleft formation and correlated fluid-rock interactions include different processes (e.g., fluid evolution, dissolution and crystallization of minerals, differential stress, etc.). The role of dissolution-precipitation during such processes is of special importance for rare earth elements (REE), which are often considered to be immobile. In addition, their transport and redistribution yield important information that potentially helps our understanding of the formation of REE ore deposits and radioactive waste deposits [e.g., *Stipp et al*., 2006; *Ewing et al*., 1995]. The concentration of actinide and REE during fluid/rock interactions depends on the fluid chemistry, the solubility of the elements, and stability of relevant REE minerals. Examples of dissolution and redistribution of REE minerals have been reported in low-grade shear zones [*Rolland et al*., 2003].

[4] In this study, we investigate a cleft formed by late transpressional dextral movements in the southwestern part of the Aar Massif in the Swiss Alps (Figure 1). Structural and mineralogical data indicate that the formation of this cleft occurred later than the Alpine metamorphic peak. Our results shed light on changes in REE mineralogy, chemical, and geological processes occurring during formation of this cleft and show that a brittle structure can be dated with hydrothermal monazite.

2. Geological Setting

[5] The Aar massif represents a polycyclic basement window belonging to the external massifs of the Alps (Figure 1). This crustal basement block is part of the European plate and was displaced under greenschist facies metamorphic conditions during late Alpine tectonics [*Bousquet et al*., 2012]. The Aar massif mainly consists of pre-Variscan gneisses, which were intruded by granites during the late to post-Variscan orogeny (~300 Ma) [e.g., *Schaltegger*, 1994].

[6] The study area is characterized by different deformation phases, which include both pre-Alpine and Alpine structures. Three Alpine deformation phases can be identified in the adjacent Mesozoic metasediments and correlated into the basement where the cleft is located (Figure 2) [*Schenker*, 1946; *Baer*, 1959; *Labhardt*, 1965; *Steck*, 1966, 1968; *Gasser and Dolivo*, 1980; *Dolivo*, 1982; *Soom*, 1986]. The first phase is only evident as a relic foliation in Mesozoic metasediments (D_1). Horizontal clefts (ZK_1) structurally related to this deformation phase are dominant north of the study area. These clefts developed late during the first deformation phase and perpendicular to the mineral lineation L_1. The second phase is the dominant deformation event in the study area, producing the transpressive shortening of the basement cover part of the western Aar massif (Figure 2). This deformation produced a main schistosity (S_2) and lineation (L_2) parallel to fold axes which plunge ~20° to SW. The metasediments underwent ductile deformation, whereas the cleft-bearing granite displays a network of brittle deformation features (e.g., brittle faults and fractures). A third deformation (D_3) produced a crenulation cleavage (S_3) in the Mesozoic metasediments (equivalent to F_{IV} of *Dolivo* [1982]). In addition, various localized faults developed. A second group of clefts (ZK_2) is oriented perpendicular to L_2 and developed late during D_2 deformation and/or during D_3 deformation.

[7] The investigated, steeply oriented ZK_2 cleft developed in a granitoid gneiss. The cleft itself dips very steeply toward NE, is several meters high, and roughly 1 m wide in the central part. It is located at the western side in the Baltschieder valley (Figure 1; near locality 1036 of *Soom* [1986]). Alpine clefts typically have complex, histories with multiple opening events. Smaller clefts and fissures (mineralized and nonmineralized) occur subparallel to the main cleft. The distance of the cleft to the Mesozoic metasediments is <100 m. The thin band of metasediments represents the hinge of a nearly isoclinal syncline (Figure 1). The axial plane of this fold can be followed from St. German toward Schiltfurgge (Figure 1). This strong asymmetric folding is coeval with dextral shearing, resulting in a new schistosity oriented parallel to the main foliation but with a subhorizontal lineation. The related dextral strike slip movements are best visible inside the granitoid gneisses. The investigated ZK_2 cleft system occurs not only in the crystalline basement but also in surrounding metasediments [e.g., *Fellenberg*, 1893; *Niggli et al*., 1940; *Steck*, 1966; *Soom*, 1986].

[8] The Alpine metamorphism is best expressed in Mesozoic metasediments. Chloritoid has been described in localities a few kilometers west of the study area [*Frey and Wieland* 1975]. The paragenesis chloritoid—chlorite—white mica indicates greenschist facies conditions during peak metamorphism of the area. This paragenesis is replaced by a lower grade metamorphic pyrophyllite-chlorite paragenesis further north [*Frey et al*., 1999]. The timing of the thermal peak is not well constrained, but shear zones that formed at similar metamorphic conditions are dated around 21.0 ± 0.2 Ma in the Grimsel area [*Rolland et al*., 2009]. After the thermal maximum was reached in southern Aar massif, a second phase of deformation is documented and dated as 14–11 Ma

Table 1. Bulk Rock Composition of Samples Around the Cleft (see Figure 1d for Locations); Major Elements in wt %, Trace Elements in Parts Per Million

	SiO_2	TiO_2	Al_2O_3	Fe_2O_3	MgO	MnO	CaO	Na_2O	K_2O	P_2O_5	LOI	Sum		
Balt5	73.61	0.07	14.70	0.84	0.36	0.01	0.20	3.30	5.46	0.09	1.2	99.86		
Balt6	73.82	0.07	14.77	0.71	0.36	bd	0.22	3.43	5.40	0.09	1.0	99.87		
Balt7	74.88	0.07	13.98	0.72	0.29	0.01	0.19	3.39	5.07	0.09	1.2	99.87		
Balt8	75.00	0.08	13.85	0.72	0.26	0.01	0.24	3.50	5.04	0.09	1.1	99.87		
Balt9	75.77	0.08	13.48	0.95	0.34	0.03	0.20	3.19	5.00	0.09	0.8	99.89		
Balt10	74.80	0.08	13.92	0.92	0.34	0.02	0.20	3.31	5.15	0.10	1.0	99.89		
	Ba	Hf	Nb	Rb	Sr	Ta	Th	U	Zr	Y	Pb			
Balt5	696	2.6	14.5	183.8	256.8	1.8	15.4	6.1	73.1	15.9	6.7			
Balt6	707	2.7	15.6	178.9	262.7	1.6	14.3	6.0	69.8	15.4	2.9			
Balt7	658	2.1	13.3	167.3	191.5	1.7	14.4	5.0	65.2	15.2	7.9			
Balt8	655	2.2	13.4	164.7	195.7	1.8	13.7	7.0	62.4	14.8	15.7			
Balt9	481	2.7	12.4	198.1	138.8	1.6	15.3	4.3	71.1	15.8	6.1			
Balt10	520	2.7	13.7	199.9	151.3	1.9	15.8	4.7	74.3	15.8	6.2			
	La	Ce	Pr	Nd	Sm	Eu	Gd	Tb	Dy	Ho	Er	Tm	Yb	Lu
Balt5	19.5	36.9	4.07	12.9	3.17	0.39	3.16	0.56	3.14	0.65	1.57	0.25	1.47	0.24
Balt6	18.0	36.0	3.94	13.2	3.31	0.38	2.79	0.53	2.89	0.56	1.63	0.24	1.26	0.19
Balt7	17.0	33.2	3.70	12.0	2.80	0.38	2.80	0.49	2.97	0.54	1.46	0.22	1.44	0.21
Balt8	14.7	30.4	3.20	11.0	2.28	0.34	2.43	0.47	2.67	0.56	1.34	0.23	1.35	0.20
Balt9	17.6	33.7	3.86	12.5	3.11	0.39	3.01	0.54	3.21	0.58	1.58	0.22	1.49	0.21
Balt10	19.9	38.0	4.23	13.8	3.22	0.40	2.95	0.53	2.74	0.56	1.65	0.23	1.65	0.23

[*Rolland et al*., 2009]. These $^{40}Ar/^{39}Ar$ ages overlap with K/Ar ages obtained on fault gouges at the southern border of the Aar massif [13–6 Ma; *Pleuger et al*., 2012].

[9] In the study area, zircon fission track ages (FT) are reset by Alpine metamorphism and show cooling below the zircon FT annealing zone (<280°C) at 8 Ma [*Michalski and Soom*, 1990]. Cooling below the partial annealing zone of FT in apatite (~120°C) occurred in the study area between 2.0 and 3.6 Ma, coeval with cooling of the Aar massif further west (southern portal of the Lötschberg base tunnel) [*Reinecker et al*., 2008].

3. Host Rock and Cleft

3.1. Host Rock Mineralogy and Bulk Chemistry

[10] The investigated country rock samples were collected at distances of 0 (Balt5 in Table 1) to 45 m from the cleft (Balt10 in Table 1 and Figure 1d). The host rock is a granite containing two feldspars, quartz, biotite, and muscovite (see also Table 1). The granitoid texture is generally preserved, even though there is greenschist facies alteration of the feldspars and biotite to white mica, albite, and chlorite. On top of this pervasive alteration, micrometer- to millimeter-sized porosity developed in several samples. These voids are the location of newly formed micrometer-scaled mineral clusters consisting of different REE minerals, white mica, and chlorite (see also below).

[11] The brownish biotite in the granite has X_{Mg} of ~0.37 and TiO_2 contents of 2.3 wt %. There are slight variations in biotite composition, most likely due to minor alteration, but only one group of biotite has been identified. The white mica can be differentiated in three groups. The two first groups have similar compositions (Table 2) but different textural characteristics. Large flakes represent primary muscovite of the granite (two mica granite). More frequent are small grains that grew inside feldspars or in foliation planes (sericite). The third group of white mica differs in texture and has a higher phengite component. These phengites are widespread and occur in cracks of older muscovite or as small, newly formed micrometer-sized platelets in voids. They have Si contents between 3.24 and 3.36 pfu (Table 2). The related celadonite exchange includes Fe and Mg (Mg# of ~0.3–0.45; Table 2 and Figure 3). The ferrimuscovite exchange is difficult to estimate, because calculated Fe^{3+} depends on the composition of the (OH) site (occupied by O in oxymicas) and the precision of the analysis (Figure 3).

[12] The bulk rock composition was measured for five samples taken at several tens of meters distance around the cleft (Figure 1d). No alteration trend was identified. All samples show very similar bulk rock chemistry despite variable alteration mineralogy and textures (Table 1 and Figure 4; Appendix).

Table 2. Mineral Composition of White Mica in the Alteration Zone of the Cleft; b.d.l.: Below Detection Limit

	Group			
	1	1	3	3
Mineral-ID	WM1	WM2	WM3	WM4
SiO_2	44.54	45.02	49.62	48.17
TiO_2	0.05	0.06	1.08	0.50
Al_2O_3	34.78	35.27	23.50	28.42
Fe_2O3	1.23	1.71	2.83	1.93
FeO	b.d.l.	b.d.l.	3.68	1.38
MnO	b.d.l.	0.04	0.06	b.d.l.
MgO	0.22	0.32	2.80	2.04
Na_2O	0.64	0.71	0.13	0.18
K_2O	10.76	10.90	11.00	11.36
H_2O	4.36	4.44	4.36	4.39
Total	7.00	7.00	7.00	7.00
Si	3.06	3.04	3.41	3.29
Ti	0.00	0.00	0.06	0.03
Al	2.82	2.81	1.90	2.29
Fe^{3+}	0.06	0.09	0.15	0.10
Fe^{2+}			0.21	0.08
Mg	0.02	0.03	0.29	0.21
Na	0.09	0.09	0.02	0.02
K	0.94	0.94	0.96	0.99
H	2.00	2.00	2.00	2.00
Total	7.00	7.00	7.00	7.00

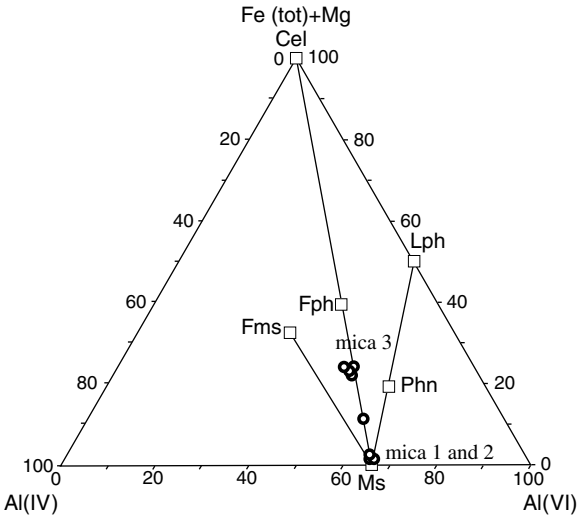

Figure 3. (Fe_{tot} + Mg)-Al^{IV}-Al^{VI} triangle for the white mica after *Giudotti* [1984]. Secondary cleft muscovites show an increased ferriphengite component (Fph). Abbreviations: Cel: celadonite; Lph: lithiophyllite; Ph: phengite; Fms: ferrimuscovite; Ms: muscovite.

3.2. REE Minerals in the Host Rock

[13] All country rock samples show a similar mineralogy of accessory REE-bearing minerals consisting of monazite, apatite, zircon, allanite, and different Y-rich minerals (see below). Two groups of monazite occur: (1) primary grains characterized by high Th and Y contents, and (2) secondary grains with low Th and U contents. Primary monazite (mnz_1) occurs as isolated, several tens of micrometer-sized grains enclosed in feldspar or quartz. This primary monazite is often overgrown by allanite (Figure 5 and Table 3). U-Th-Pb electron microprobe (EMP) chemical dating of these monazite grains indicates a Variscan age. These primary minerals have partly survived the Alpine evolution as relics inside the investigated alteration zone. In addition to relics of primary monazite, a second group of monazite (mnz_2) occurs as small, irregular tens of micrometer-sized grains. They are lower in Th and U than mnz_1 and fall in the field of hydrothermal monazites as defined by *Janots et al*. [2012]. The measured Th/U values are, however, slightly different from the cleft monazite (Table 3). Small thorite grains (~1–5 µm) are common in the immediate vicinity of such monazites. Allanite is the most common light REE phase. It occurs as overgrowths on mnz_1, as isolated, 100 µm-sized irregular grains, and as grain aggregates. The latter are mainly found in biotite clusters. Some larger grains show minor zoning in backscattered images, but most allanite grains are relatively homogeneous. Small alteration rims around allanite have been observed containing higher Th contents. These rims are only 0.5 to 1 µm thick.

[14] Y-rich, Si-bearing minerals containing REE (Table 4 and Figures 5 and 6) occur as isolated grains in open voids or as small grains together with other accessory minerals (Figure 5) in the cleft wall host rock. The minerals are 2 to 50 µm in size and sometimes zoned (Figure 5d). Investigatory analyses indicate that they are either Y-Si-oxides/hydroxides (e.g., tombarthite, $Y_4(Si_4H_4)O_{12-x}(OH)_{4+2x}$; thalénite-(Y), $Y_3Si_3O_{10}OH$; yttrialite-(Y), $(Y, Th)_2Si_2O_7$), carbonates (e.g., iimoriite-(Y),$Y_2(SiO_4)(CO_3)$), or Be-containing silicates (e.g., hingganite-Y, $BeYSiO_4(OH)$; gadolinite, $Y_2FeBe_2Si_2O_{10}$). The sums of the analyses (Table 4) suggest a best fit with a carbonate. In contrast, the measured Si/(Y + REE) ratios of ~1.2 are more indicative of oxides/hydroxides than carbonates. A comparable occurrence of a secondary REE mineral in shear zones of the Mont Blanc massif has been interpreted as tombarthite [*Rolland et al*., 2003]. In the following, we will use "tombarthite" in the text to indicate the uncertainty of the mineral name. These Y-Si minerals are the dominant Y-phase in the alteration zone. EMP data of this mineral show ΣREE between 17 and 22 wt % with an enrichment in middle REE (Figure 6). A second important secondary Y-phase is a Y-Nb-Ti mineral. The stoichiometry indicates a mineral of the pyrochlore or aeschynite group (Table 5), for example yttropyrochlore, $(Y,Na,Ca,U)_{1-2}(Nb,Ta,Ti)_2(O,OH)_7$ or aeschynite-(Y), $(Y,Ca,Fe,Th)(Nb,Ti)_2(O,OH)_6$. This Y-phase occurs as small grains in voids, in the immediate vicinity of ilmenite grains (Figure 5). Such minerals are commonly seen in retrograde systems [e.g., *Rolland et al*., 2003; *Regis et al*., 2012] and are often interpreted as aeschynite, although the distinction between yttropyrochlore and aeschynite is difficult to establish without diffraction data. The high Nb content of these minerals requires an Nb source during alteration,

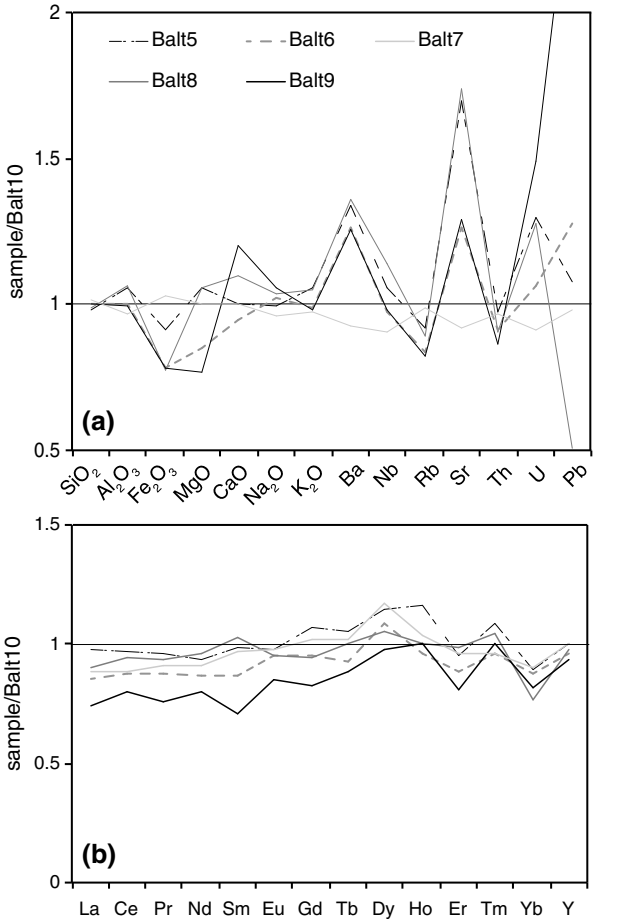

Figure 4. Whole rock chemistry of variably altered country rocks. (a) Selected major and trace elements normalized to the freshest sample (Balt10). (b) Same as Figure 4a but for the REE.

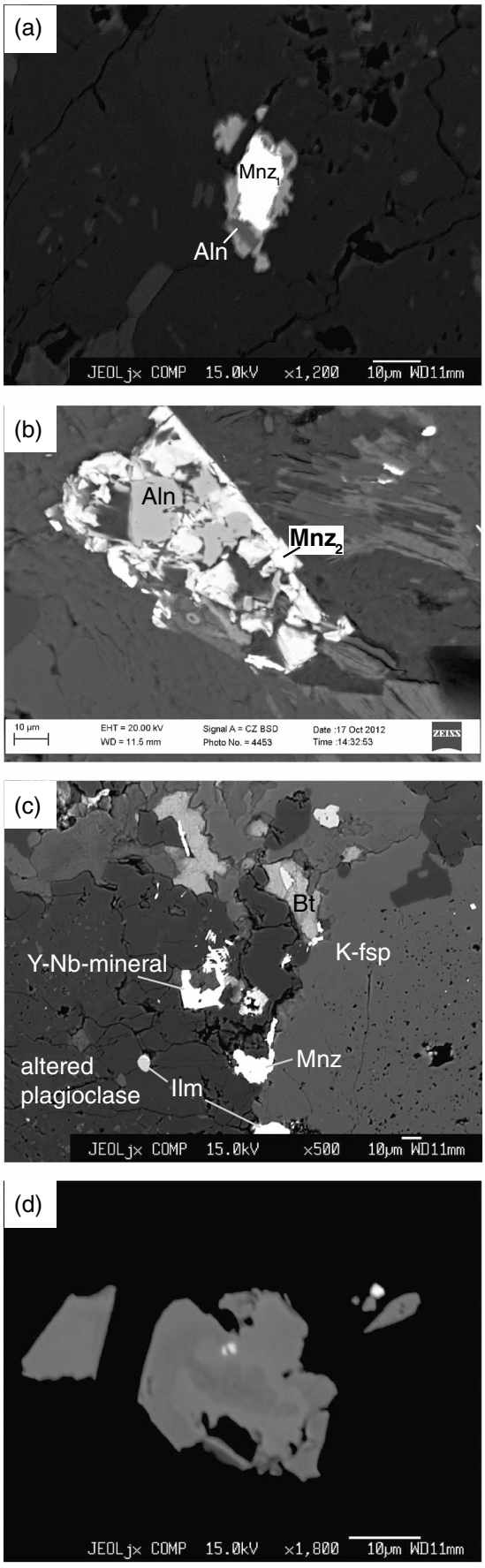

Figure 5. BSE images documenting REE mineral reactions in the alteration zone. (a) Example of monazite$_1$ overgrown by allanite. (b) Monazite$_2$ replacing allanite. (c) Textural relationships of aeschynite/prochlore minerals. Note also other accessory minerals. (d) Example of a Y-Si mineral ("tombarthite") displaying internal zonation.

which is most likely derived from the ilmenite of the granite. The alteration of ilmenite can also be related to formation of TiO_2 phases (anatase, brookite, rutile) in the alteration zone and the cleft.

3.3. Cleft Mineral Association

[15] The mineral content of the investigated ZK_2 cleft is dominated by quartz, adularia, albite, chlorite, and TiO_2 minerals (predominantly anatase, followed by rutile) and ilmenite. Apatite, xenotime, and bertrandite have also been found in the investigated cleft [*Stalder*, 1990; Paul Bähler, pers. comm.]. Brookite and ilmenite have been reported from two out of three monazite-bearing clefts in the vicinity [*Soom*, 1986]. In the studied cleft, monazite crystallizes at a late stage (at the very end of adularia and quartz crystallization), together with anatase. Monazite is the dominating cleft REE mineral. Allanite does not form part of the cleft mineral association.

4. Cleft Monazite

4.1. Monazite Composition

[16] Monazites are slightly pinkish and 1–2 mm in size. The cleft monazite composition is typical of hydrothermal setting [*Mannucci et al*., 1986; *Janots et al*., 2012] with ThO_2 contents between 0.8 and ~3 and <0.05 wt % UO_2 contents. The Y_2O_3 contents are around 0.5 wt %. The Th/U ratio varies between 30 and 215. These values are considerably higher than values found in high- and medium-grade monazites in rocks (average Th/U values: 3–7) [*Janots et al*., 2008, 2012]. The composition and REE pattern of the low-grade monazite (mnz_2) in the country rock and the clefts are equivalent (Table 3). However, the cleft monazites display different growth zones with varying Th content.

4.2. Th-U-Pb SIMS Results

[17] We analyzed the visible growth domains of two monazite crystals grown on cleft quartz. BALT4 is partly enclosed in quartz, whereas BALT2 grew on the surface of quartz. For both grains, SIMS Th-U-Pb dating was performed at multiple locations on central sections of the two grains (Figures 7 and 8 and Table 6 and 7). ^{232}Th-^{208}Pb dating was preferred to U-Pb dating due to significant contribution of common Pb and ^{206}Pb excess in Alpine cleft monazite [*Gasquet et al*., 2010; *Janots et al*., 2012]. The uncorrected U-Pb data contain different Pb components, which can be identified in a Tera-Wasserburg diagram (Figure 9). The main contributors to Pb concentrations are common and radiogenic Pb components and an additional excess Pb component (Figure 9).

[18] In BALT2, different domains can be distinguished based on Th-U composition and texture (Figure 7). A zone with a low backscattered electron (BSE) contrast yields relatively old ages and represents the core of the grain, with a ^{232}Th-^{208}Pb weighted mean age of 8.03 ± 0.22 Ma

Table 3. Composition of REE Minerals (Oxide are Given in wt %); n.a.: Not Analyzed; b.d.l.: Below Detection Limit

	Sample						
	Balt9	Balt9	Balt9	Balt9	Balt5	BALT2	BALT2
Mineral	Aln	Aln	Mnz_1	Mnz_1	Mnz_2	Mnz cleft	Mnz cleft
P_2O_5	0.10	0.05	31.31	31.95	31.82	31.38	31.17
SiO_2	29.77	29.94	0.51	0.35	0.13	0.10	0.10
ThO_2	0.11	0.01	6.63	6.92	0.64	1.37	0.69
UO_2	b.d.l.	b.d.l.	0.41	0.68	0.03	0.01	0.06
Al_2O_3	17.75	16.62	b.d.l.	b.d.l.	b.d.l.	0.05	0.04
FeO	12.59	12.93	b.d.l.	b.d.l.	b.d.l.	b.d.l.	b.d.l.
MgO	0.19	0.13	n.a.	n.a.	n.a.	n.a.	n.a.
CaO	10.87	10.17	1.22	1.54	0.55	b.d.l.	b.d.l.
La_2O_3	5.41	5.80	15.47	14.98	16.47	16.11	16.20
Ce_2O_3	11.66	12.05	30.06	28.67	33.47	32.10	33.15
Pr_2O_3	1.03	1.30	2.73	2.95	3.46	3.03	3.13
Nd_2O_3	3.51	4.31	10.57	9.92	11.57	11.17	10.34
Sm_2O_3	0.59	0.62	1.50	1.55	2.10	1.75	1.74
Gd_2O_3	0.31	0.26	0.85	1.08	1.12	0.94	0.80
Dy_2O_3	b.d.l.	0.04	0.05	b.d.l.	b.d.l.	0.03	0.11
Y_2O_3	0.44	0.34	1.06	1.43	0.99	0.58	0.68
Sum	94.323	94.566	102.373	102.021	102.677	98.63	98.21

(mean square weighted deviation (MSWD) = 0.33 analyses 27–29; Figure 8). In the central part of the grain, two domains show variable Th contents at comparable U concentrations (Figure 7). The ^{232}Th-^{208}Pb ages of these two growth domains largely overlap. The weighted mean ^{232}Th-^{208}Pb age of the older domain is 6.60 ± 0.18 Ma (MSWD = 3.3; analyses 8–25; average Th/U: 58). A rim domain (analyses 1–7) has high Th/U ratio (> 130; average: 163) and yields a weighted mean ^{232}Th-^{208}Pb age of 6.32 ± 0.20 Ma (MSWD = 1.4). At the interface between the central part and rim domains, analysis spots 30–33 give intermediate signatures with respect to Th/U and cannot be attributed to one specific growth domain.

[19] In the smaller BALT4 grain, ^{232}Th-^{208}Pb ages indicate a more complex 3-D zoning. Analysis spot 16 represents a mixed analysis obtained on the rim. The core region of the grain consists of three age domains that are correlated with different Th/U ranges (Figure 8). The oldest domain (analysis 1, 4–9, 13–15) yield an average age of 7.71 ± 0.40 Ma (MSWD = 7.4; average Th/U ratio: 99). The second group (17, 19–21, 26) has a weighted mean of 7.40 ± 0.17 Ma (MSWD = 0.95; average Th/U ratio: 54). The region displaying a lighter BSE contrast (spots 2–3 and 10–12; Figure 7) gives an age of 6.49 ± 0.25 Ma (MSWD = 1.4). The youngest analysis spots (18, 22–24) are found in the upper left rim in Figure 6 showing low Th/U ratios (average: 24). They yield an average age of 6.25 ± 0.60 Ma (MSWD = 5.5). Analysis 25 represents an isolated age spot with high Th/U ratio and high Th content (bright zone in Figure 7), and most likely includes exsolution of a Th-phase.

Table 4. Composition of Y-Si Minerals[a]

SiO_2	26.92	27.36	25.04	26.31
La_2O_3	0.09	0.34	0.31	0.16
Ce_2O_3	1.65	2.60	1.28	2.67
Pr_2O_3	0.12	0.59	0.44	1.06
Nd_2O_3	3.49	3.63	2.65	5.55
Sm_2O_3	2.37	1.86	2.01	2.83
Gd_2O_3	4.55	3.80	4.41	4.11
Dy_2O_3	4.82	4.43	3.85	3.24
Ho_2O_3	0.00	0.86	0.86	0.46
Er_2O_3	1.51	1.13	0.64	0.79
Yb_2O_3	1.39	1.41	1.00	1.17
Y_2O_3	28.92	30.06	28.64	27.99
FeO	7.30	5.68	7.55	5.56
CaO	1.62	3.01	1.71	2.48
Sum meas.	**84.75**	**86.76**	**80.39**	**84.39**
CO2	*13.9*	*14.2*	*13.3*	*13.7*
Total	*98.6*	*101.0*	*93.7*	*98.1*

[a](Oxides are given in wt %). The calculated amount of CO_2 are given for Iimorite (see text).

5. Discussion

5.1. Ages

[20] The isotope data show different amounts of excess Pb components (Figure 9) and different age domains with analytically reproducible ages (low MSWD). In the monazites studied, the weighted mean ^{232}Th-^{208}Pb ages of individual growth domains generally overlap within error. This is often used as a criterion to calculate an average age for an entire grain. However, we know from fluid inclusions that cleft mineral crystallization is a stepwise process [e.g., *Sharp et al*., 2005], which can also include dissolution steps. For this reason it makes little sense to present an average crystallization age for an entire grain. With respect to brittle deformation, our data indicate that cleft formation occurred slightly before 8.03 ± 0.22 Ma and that monazite growth continued until 6.25 ± 0.60 Ma (Table 8). Some age domains show

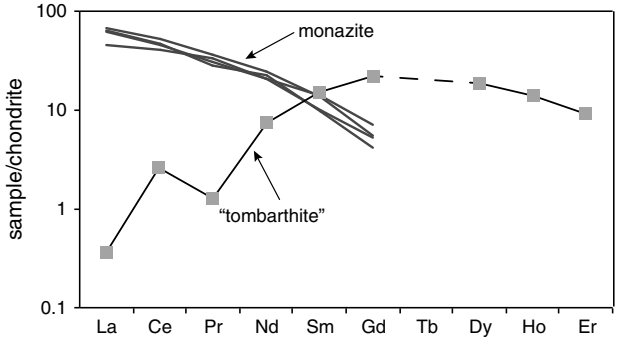

Figure 6. REE pattern of Si-Y minerals and monazite forming in the cleft wall due to fluid-rock interaction (see Table 4 for data).

Table 5. Composition of Y-Nb Minerals[a]

	Sample			
	Balt9	Balt9	Balt9	Balt9
ID	TiNb1	TiNb2	TiNb4	TiNb6
Nb_2O_5	32.69	27.87	27.87	30.31
Ta_2O_5	3.20	0.99	2.00	1.99
ThO_2	1.57	2.34	2.21	2.26
UO_2	5.21	3.18	3.72	4.01
SiO_2	1.15	5.91	4.71	2.55
TiO_2	22.73	24.16	24.84	25.81
La_2O_3	b.d.l.	0.06	b.d.l.	b.d.l.
Ce_2O_3	n.a.	0.19	0.07	0.17
Nd_2O_3	n.a.	0.11	0.52	0.29
Y_2O_3	12.94	14.33	13.98	18.80
FeO	0.93	0.99	0.40	0.48
CaO	1.45	0.54	0.37	0.37
Sum	81.86	80.664	80.696	87.032

[a](Oxides are given in wt %); n.a.: not analyzed; b.d.l.: below detection limit.

homogeneous compositions, textural positions, and ages (e.g., rim of BALT2, core1 of BALT4), whereas others are less homogeneous; the latter is expressed by elevated MSWD values.

5.2. Monazite, Allanite, and Y-Mineral Forming Reactions

[21] The investigated country rocks of the cleft show a network of brittle deformation planes. According to *Soom* [1986], the hydrous fluid in ZK_2 clefts typically contains 4.2–7.6 wt % NaCl equivalent and <2 mol% CO_2. However, there is no obvious variation in bulk rock composition of the cleft wall rock with distance to the cleft (Table 1). This is in contrast to shear zones in granitic rocks studied in the Mont Blanc massif [*Rolland et al*., 2003], where changes in REE mineralogy are associated with significant changes in bulk rock REE concentrations. The most pervasive transformation is connected to greenschist facies Alpine metamorphism, which is responsible for allanite growth (+ new rock-forming minerals) at the expense of monazite [e.g., *Janots et al*., 2008] (Figure 5) and can be summarized with reactions of the type:

$$\text{monazite}_1 + \text{plagioclase} + \text{fluid}_1 \Rightarrow \text{allanite} + \text{fluid}_2 \quad (1)$$

[22] This is indicated by the EMP Variscan age of monazite relics (mnz_1) and the reaction texture of monazite replaced by allanite (Table 3 and Figure 5). Additional mineral changes in granite are caused by hydrothermal fluid-induced reactions during deformation of the granite superimposed on the low-grade Alpine metamorphic assemblages. The second type of reaction in the granite is characterized by the growth of various new REE-bearing phases in the alteration zone and the cleft (Figure 5): (1) formation of $monazite_2$ from allanite, (2) development of the Y-Si minerals (tombarthite), and (3) development of Y-Nb-Ti minerals (pyrochlore/aeschynite).

[23] TiO_2 (anatase, brookite) and $ThSiO_4$ (thorite) form in association with this alteration. One possible reaction to form $monazite_2$ from allanite is

$$\text{allanite} + \text{apatite} \Rightarrow \text{monazite}_2 + \text{chlorite} + \text{fluid(including Ca)} \quad (2)$$

[24] This reaction occurs in the host rock but is probably also linked to the formation of cleft monazite. By comparing allanite and newly formed monazite compositions, there is excess in Y, Th, and U (if reaction (2) is balanced for Ce). The incompleteness of reaction (1) allows also direct reactions to form $monazite_2$ from $monazite_1$:

$$\text{monazite}_1 \Rightarrow \text{monazite}_2 \quad (3)$$

[25] Reaction (3) would also be a source of Y and Th (but not Nb). This reaction is considered unimportant due to the

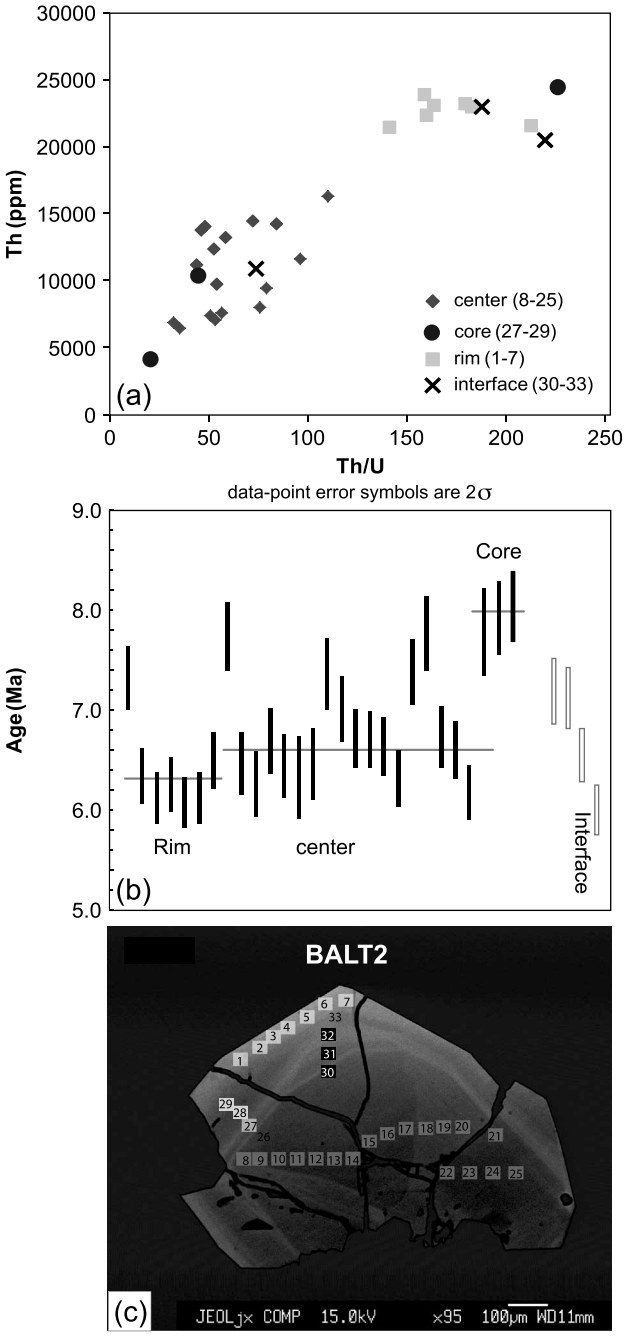

Figure 7. Th/Pb systematics and ages of grain BALT2. (a) Th/U versus Th concentrations indicting different zones (see also Figures 7b and 7c). (b) $^{232}Th/^{208}Pb$ ages. (c) BSE image of BALT2 with locations of the spots and analysis numbers (Table 6).

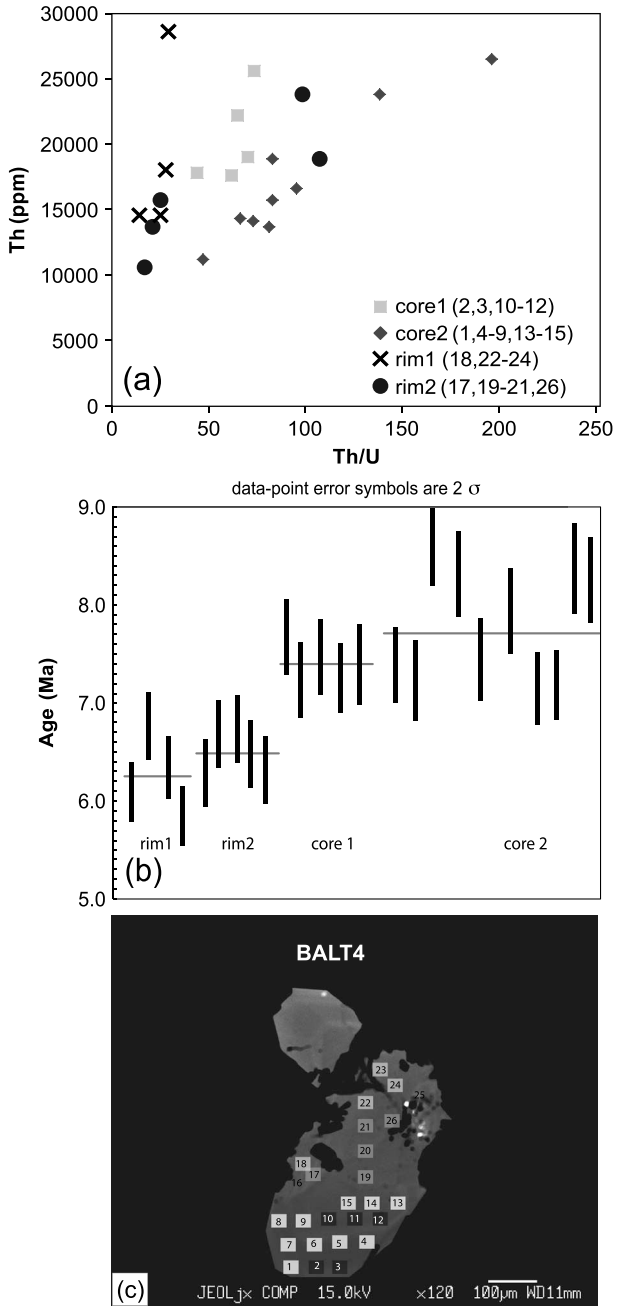

Figure 8. Th/Pb systematics and ages of grain BALT4. (a) Th/U versus Th concentrations indicting different zones. (b) $^{232}Th/^{208}Pb$ ages. (c) BSE image of BALT4 with locations of the spots and analysis numbers (Table 7).

low amount of monazite$_1$ relics. The two proposed reactions could account for the crystallization of the Y-rich minerals in the host rock. A common Y source in granitoids for the Y-Si- and Y-Nb-Ti minerals would be xenotime.

5.3. Cleft Formation in a Geological Context

[26] Isotopic analyses of two cleft monazites yield similar $^{208}Pb/^{232}Th$ ages of 6–8 Ma (see section on Th-U-Pb SIMS results; Table 8). As discussed in the geological setting, the clefts developed perpendicular to L_2 and in the late stages of the D_2 deformation and during D_3 deformation (Figure 2). The regional stress field controls the relationship between shortening directions and opening of the cleft. In this context, the main foliation (S_2) can be interpreted as plane perpendicular to maximum stresses, whereas the opening direction of the cleft would be the direction of the minimum stresses. All these data are compatible with a stress field for D_2 deformation (Figure 10). In addition, the maximum stress direction for the finite deformation of D_3 rotates around ~45° (Figure 10) [*Dolivo*, 1982]. Also, available orientations of ZK_2 clefts [*Soom*, 1986] allow a minor rotation of the maximum stress field between D_2 and D_3 (Figure 10). In any case, the intermediate stress axes have to be close to vertical. This is a situation characteristic of strike slip movements and is also consistent with observed kinematic indicators (e.g., rotated clasts, shear bands). Other ductile, dextral strike slip to locally dip-slip shear zones in the Grimsel area of the Aar Massif (~40 km to the NE) were active between ~14 and 12 Ma ($^{40}Ar/^{39}Ar$ white mica ages; stage 2 of *Rolland et al*. [2009]; Table 8). Moreover, at the southern border of the Aar massif near the village of Baltschieder, phyllonites have been related to the activity of the dextral Rhone-Simplon line (Figure 1) [*Campani et al*., 2010, and references therein]. These phyllonites (mylonites) yielded white mica $^{40}Ar/^{39}Ar$ ages between 13.7 ± 0.1 and 11.0 ± 0.1 Ma [*Campani et al*., 2010] (for sample localities, see Figure 1). Some of these dated shear zones may be related to the stress field that caused formation of ZK_2 clefts.

[27] *Campani et al*. [2010] indicate overall fault activity between 20 and 3 Ma along the Rhone-Simplon line, whereas the well-documented and dated telescoped crustal section occurs along the normal fault segment (Simplon line sensu strictu). This deformation occurred continuously and over ~15 Ma. The strike slip part of the Rhone-Simplon line has an intermediate N-dipping orientation. In contrast, the planes of the D_2 deformation with dextral movements dip to the NNW (Figure 10). The age difference of 4–6 Ma between the $^{40}Ar/^{39}Ar$ age of the phyllonites near Baltschieder [*Campani et al*., 2010] (Figure 1 and Table 8) and the cleft monazites investigated here may be interpreted in the following ways:

[28] 1. The white mica ages in mylonites record a small time window in a continuous ductile deformation event and can be disturbed by excess Ar. The latter is excluded in modern Ar studies of shear zones where a complete resetting of micas at least in the presence of water is indicated [e.g., *Rolland et al*., 2008; *Sanchez et al*., 2011].

[29] 2. The white mica Ar ages date the earlier, higher temperature evolution of a continuous deformation process and the cleft monazites growth during the late brittle stage.

[30] 3. The two data sets are not directly comparable, because the slight divergence in orientations of the dated structures.

[31] In any case, the data indicate ongoing deformation during the lower Miocene within and at the border of the Aar massif (Figure 1 and Table 8). The later deformation is consistent with the brittle deformation further NE along brittle fault planes [*Pleuger et al*., 2012].

[32] The timing and conditions of deformation responsible of ZK_2 cleft formation can be compared with available thermochronological data from the literature. $^{40}K/^{40}Ar$ dating of adularia from a neighboring, parallel cleft (locality 1036 in *Soom* [1986]) yielded maximum crystallization ages of 13.0 ± 1.0 Ma, due to recorded Ar overpressure. This age thus

Table 6. SIMS U-Th-Pb Isotopic Ratios and Th/Pb Ages in BALT2 Monazite Domains

Analysis ID	[U] ppm	[Th] ppm	Th/U Means	$^{207}Pb/^{235}U$	±σ %	$^{206}Pb/^{238}U$	±σ %	$^{207}Pb/^{206}Pb$	±σ %	$^{232}Th/^{208}Pb$ uncorr.	±σ %	$^{232}Th/^{208}Pb$ Age (Ma) uncorr	±σ Ma	$^{232}Th/^{208}Pb$ Age (Ma) corrected	±σ Ma
group 1															
n4190-balt2@1	121	24516	202	0.037211	8.6	0.00238	2.9	0.113	8.1	0.00037	2.5	7.48	0.19	7.37	0.19
n4190-balt2@02	150	26111	174	0.033865	9.6	0.00221	4.8	0.111	8.3	0.00032	2.5	6.57	0.16	6.47	0.17
n4190-balt2@03	180	27159	151	0.033824	9.8	0.00215	2.9	0.114	9.3	0.00031	2.5	6.26	0.16	6.20	0.16
n4190-balt2@04	169	26242	156	0.036721	9.9	0.00213	3.6	0.125	9.2	0.00032	2.5	6.38	0.16	6.36	0.16
n4190-balt2@05	182	24382	134	0.035546	10.1	0.00216	3.6	0.119	9.4	0.00031	2.5	6.25	0.16	6.14	0.15
n4190-balt2@06	167	25411	152	0.033564	9.6	0.00229	2.8	0.106	9.1	0.00031	2.5	6.29	0.16	6.20	0.16
n4190-balt2@07	155	26382	171	0.064678	7.1	0.00274	2.9	0.171	6.5	0.00034	2.5	6.82	0.17	6.64	0.17
group 2															
n4190-balt2@08	179	18771	105	0.038552	7.0	0.00161	3.3	0.174	6.1	0.00040	2.6	8.05	0.21	7.77	0.21
n4190-balt2@09	271	8115	30	0.035443	11.6	0.00132	3.5	0.195	11.1	0.00034	2.6	6.78	0.18	6.47	0.19
n4190-balt2@10	227	7579	33	0.056827	7.6	0.00151	3.6	0.274	6.7	0.00033	2.7	6.68	0.18	6.27	0.19
n4190-balt2@11	176	8591	49	0.117577	7.9	0.00196	3.0	0.435	7.3	0.00035	2.8	7.12	0.20	6.71	0.19
n4190-balt2@12	173	8401	49	0.131776	6.2	0.00224	2.8	0.426	5.5	0.00037	2.7	7.38	0.20	6.30	0.19
n4190-balt2@13	164	8765	53	0.183737	5.5	0.00264	2.4	0.504	4.9	0.00039	2.6	7.84	0.21	6.41	0.25
n4190-balt2@14	156	7873	51	0.209309	5.4	0.00291	2.7	0.521	4.7	0.00039	2.8	7.92	0.22	6.48	0.21
n4190-balt2@15	130	9339	72	0.210702	4.7	0.00303	2.2	0.505	4.1	0.00043	2.8	8.75	0.24	7.39	0.21
n4190-balt2@16	145	10800	75	0.255286	4.8	0.00338	2.4	0.548	4.2	0.00041	2.7	8.35	0.23	6.96	0.20
n4190-balt2@17	145	13234	91	0.319171	4.5	0.00414	2.4	0.560	3.8	0.00039	2.6	7.95	0.20	6.62	0.18
n4190-balt2@18	240	16432	68	0.068033	6.2	0.00171	2.6	0.289	5.6	0.00035	2.5	7.02	0.18	6.60	0.17
n4190-balt2@19	283	14055	50	0.054750	6.8	0.00161	2.5	0.247	6.4	0.00033	2.5	6.74	0.17	6.52	0.18
n4190-balt2@20	272	15034	55	0.049453	7.4	0.00165	4.1	0.217	6.2	0.00033	2.6	6.74	0.17	6.40	0.17
n4190-balt2@21	203	16186	80	0.063941	8.7	0.00171	3.8	0.271	7.9	0.00038	2.6	7.65	0.20	7.38	0.20
n4190-balt2@22	217	11068	51	0.057909	5.5	0.00172	2.7	0.244	4.8	0.00041	2.8	8.24	0.23	7.80	0.22
n4190-balt2@23	307	12709	41	0.054112	7.2	0.00155	2.4	0.253	6.8	0.00035	2.5	7.03	0.18	6.74	0.18
n4190-balt2@24	359	15658	44	0.040144	6.7	0.00141	2.4	0.206	6.3	0.00033	2.5	6.76	0.17	6.62	0.17
n4190-balt2@25	351	15963	45	0.037841	6.9	0.00134	2.5	0.204	6.5	0.00033	2.7	6.57	0.17	6.17	0.16
group 3															
n4190-balt2@27	244	4697	19	0.017592	10.6	0.00137	3.8	0.093	9.9	0.00040	2.9	8.07	0.23	7.89	0.26
n4190-balt2@28	280	11703	42	0.027628	6.9	0.00159	3.3	0.126	6.1	0.00041	2.6	8.34	0.22	8.05	0.22
n4190-balt2@29	129	27749	215	0.047408	7.3	0.00255	2.8	0.135	6.7	0.00042	2.6	8.43	0.22	8.19	0.21
interface															
n4190-balt2@26	172	13984	81	0.040268	7.4	0.00181	3.2	0.161	6.7	0.00041	2.6	8.32	0.22	7.95	0.21
n4190-balt2@30	177	12377	70	0.078766	6.5	0.00192	2.9	0.298	5.8	0.00038	2.7	7.74	0.21	7.18	0.20
n4190-balt2@31	111	23289	209	0.132868	7.2	0.00262	4.5	0.368	5.6	0.00036	2.5	7.32	0.19	7.11	0.18
n4190-balt2@32	146	26116	179	0.066765	8.3	0.00186	2.5	0.261	7.9	0.00033	2.5	6.59	0.16	6.42	0.16

Table 7. SIMS U–Th–Pb Isotopic Ratios and Th/Pb Ages in BALT4 Monazite Domains

Analysis ID	[U] ppm	[Th] ppm	Th/U Means	$^{207}Pb/^{235}U$	±σ %	$^{206}Pb/^{238}U$	±σ %	$^{207}Pb/^{206}Pb$	±σ %	$^{232}Th/^{208}Pb$ uncorr.	±σ %	$^{232}Th/^{208}Pb$ Age (Ma) uncorr	±σ Ma	$^{232}Th/^{208}Pb$ Age (Ma) corrected	±σ Ma
group 1															
n4191-balt4@1	173	23994	139	0.077888	6.9	0.00216	2.9	0.261	6.2	0.00038	2.7	7.75	0.21	7.39	0.20
n4191-balt4@04	237	11410	48	0.032843	7.0	0.00136	2.8	0.176	6.4	0.00037	2.7	7.52	0.21	7.23	0.20
n4191-balt4@06	135	26463	196	0.060890	10.9	0.00229	5.3	0.193	9.5	0.00042	2.6	8.41	0.22	8.31	0.22
n4191-balt4@07	218	14365	66	0.128556	6.9	0.00237	3.6	0.393	5.9	0.00040	2.6	7.98	0.21	7.45	0.20
n4191-balt4@08	168	13629	81	0.130330	5.2	0.00240	2.6	0.393	4.6	0.00043	2.7	8.74	0.24	7.95	0.22
n4191-balt4@09	175	16599	95	0.205562	5.3	0.00324	2.4	0.461	4.7	0.00039	2.5	7.80	0.20	7.15	0.18
n4191-balt4@13	353	36899	105	0.032711	5.9	0.00150	2.2	0.158	5.5	0.00036	2.5	7.34	0.18	7.20	0.18
n4191-balt4@14	192	15818	82	0.063748	7.0	0.00185	3.3	0.251	6.1	0.00042	2.6	8.53	0.23	8.38	0.23
n4191-balt4@15	230	19167	83	0.075226	7.6	0.00193	3.8	0.282	6.5	0.00042	2.6	8.47	0.22	8.25	0.22
group 2			99												
n4191-balt4@17	647	13791	21	0.020862	4.9	0.00135	2.1	0.112	4.5	0.00038	2.6	7.72	0.20	7.39	0.20
n4191-balt4@19	180	19561	108	0.104726	5.3	0.00221	2.4	0.343	4.8	0.00040	2.5	8.01	0.20	7.68	0.19
n4191-balt4@20	640	15984	25	0.034371	4.1	0.00146	1.7	0.171	3.8	0.00039	2.6	7.91	0.20	7.23	0.19
n4191-balt4@21	642	10682	17	0.026349	4.3	0.00137	1.6	0.139	4.0	0.00039	2.6	7.79	0.20	7.47	0.20
n4191-balt4@26	245	24157	99	0.413087	2.9	0.00496	1.5	0.604	2.6	0.00041	2.5	8.31	0.21	7.26	0.17
group 3			54												
n4191-balt4@18	981	28648	29	0.026877	7.4	0.00138	2.2	0.141	7.0	0.00031	2.5	6.27	0.16	6.11	0.15
n4191-balt4@22	610	14844	24	0.034611	4.3	0.00137	1.4	0.183	4.1	0.00036	2.5	7.36	0.18	6.77	0.17
n4191-balt4@23	645	18118	28	0.134097	3.3	0.00233	1.4	0.417	3.0	0.00037	2.6	7.43	0.19	6.33	0.16
n4191-balt4@24	1073	14622	14	0.068978	4.1	0.00172	1.7	0.292	3.7	0.00034	2.7	6.83	0.18	5.86	0.16
group 4			24												
n4191-balt4@02	286	17792	62	0.040242	9.2	0.00154	3.7	0.190	8.5	0.00033	2.5	6.59	0.17	6.30	0.16
n4191-balt4@03	270	19112	71	0.036579	7.4	0.00157	2.8	0.169	6.9	0.00034	2.5	6.79	0.17	6.69	0.17
n4191-balt4@10	341	22240	65	0.049253	11.0	0.00165	2.7	0.216	10.7	0.00034	2.7	6.77	0.18	6.71	0.18
n4191-balt4@11	405	17892	44	0.040734	12.7	0.00148	5.9	0.200	11.2	0.00032	2.6	6.46	0.17	6.47	0.18
n4191-balt4@12	347	25791	74	0.035109	9.4	0.00161	2.7	0.159	9.0	0.00032	2.6	6.40	0.16	6.31	0.16
interface															
n4191-balt4@16	539	6015	11	0.156070	3.5	0.00261	1.4	0.433	3.2	0.00062	2.7	12.51	0.34	9.18	0.30
n4191-balt4@25	393	52194	133	0.064994	5.3	0.00178	2.3	0.264	4.7	0.00033	2.5	6.68	0.17	6.52	0.16

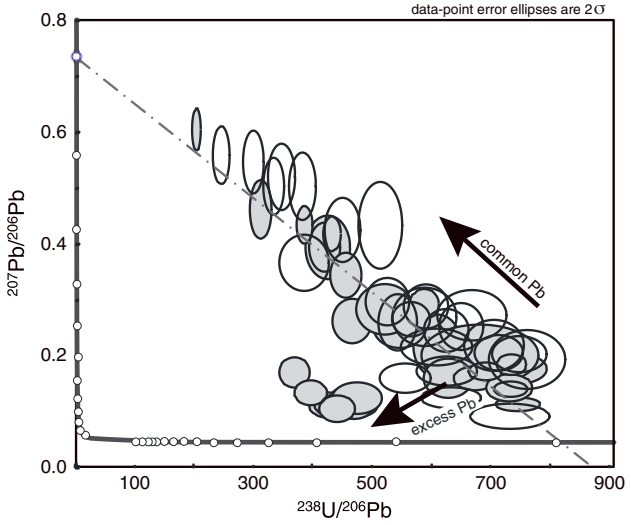

Figure 9. Uncorrected U-Pb Tera-Wasserburg diagram for cleft monazite. Note the two different components of the Pb isotopes (common and excess Pb) [see *Janots et al*., 2012 for discussion]. Filled ellipses: BALT2; open ellipses: BALT4.

provides a conservative maximum age of the ZK_2 cleft adularia crystallization, which starts shortly after cleft formation. The adularia rim dating of 10.5 ± 1.0 Ma provides a maximum age for the final crystallization of adularia. Two additional groups of data are available: (1) Zircon FT ages, and (2) fluid inclusion data. The available zircon FT ages of 8 Ma [*Michalski and Soom*, 1990] are similar or older than the dated cleft monazites. Therefore, the cleft monazite formed at or below conditions of zircon FT annealing zone. The absolute temperatures for the partial annealing zone of zircon FT are under discussion, but all different data sets indicate temperatures below 280°C [e.g., *Yamada et al*., 1995; *Bernet*, 2009].

[33] Available isochores from fluid inclusions in quartz from a parallel cleft indicate quartz crystallization at 220°C–280°C and ~0.8 kbar [*Soom*, 1986]. Recall that cleft monazite growth starts when quartz and adularia growth ceases. The PT conditions are calculated from measured isochores and an assumed thermal gradient. The isochores have an uncertainty related to the volume estimate of the fluid inclusion (optical estimates) and the assumed and thermal gradient. However, the PT estimates from ZK_1 fluid inclusions are consistent with peak metamorphic conditions indicated by the mineral paragenesis observed in rocks and a 30°C/km lithostatic gradient. For this reason, the temperature estimate obtained from fluid inclusion data of ZK_2 is considered to be robust. Physical conditions below 280°C for the cleft formation are in agreement with the fluid inclusion data, the FT data, and ductile deformation in metasediments while brittle deformation prevails in the crystalline basement. The structures and the physical conditions represent the final stage of the major deformation. This occurs during the retrograde history including cooling and exhumation of the western Aar massif. Whether the rim crystallization of BALT2 is caused by the D_3 deformation of the D_2 cleft needs to be confirmed with analyses of monazite from a D_3 cleft.

6. Summary and Conclusion

[34] The presented example shows the potential to date or constrain brittle deformation with monazite crystallization ages. The monazite Th/Pb system is not influenced by later diffusion; therefore, it provides additional information to fission track data. High precision of individual data points is only possible in large crystals occurring in clefts. The method is even more powerful if it can be combined with fluid evolution data. However, in combination with structural analysis and cleft mineral growth sequence, the ages provide new insights into the timing and evolution of brittle deformation in orogenic basement.

[35] The investigated cleft represents such an example, where deformation and Alpine exhumation/cooling models derived from FT data can be combined. Cleft formation is correlated with alteration and growth of new minerals in the country rock. Minerals crystallizing in the cleft (quartz, adularia, chlorite) have also been found in pores of the cleft wall rock. The NaCl bearing brine filling the cleft has the capability of redistributing actinides, REE, and Y in the country rock. This is most likely related to the ligands of such fluids [e.g., *Rolland et al*., 2003; *Janots et al*., 2012]. The newly formed carbonates in the country rocks indicate a certain amount of CO_2 in the water-dominated fluid. The retrograde character of the alteration and the cleft exclude a local fluid source (i.e., the granite itself). Therefore, the fluid flow is largely a result of local alteration and probably includes elements derived from nearby metasediments (Figure. 1).

[36] The investigated cleft monazite crystals give a lower age limit for mineral growth in this cleft, lasting from 8.03 ± 0.22 to 6.25 ± 0.60 Ma (Table 8). They also yield an estimate of the time when brittle deformation started in competent lithologies in the shear zone. The overall stress field can be summarized to final stages of dextral movements along steep NNW dipping planes. The orientation and

Table 8. Summary of Ages, Dating Deformation Stages in the Area

Age group	Age [Ma]	Error [Ma]	Grain/Sample	Method	Reference
Monazite (core)	8.03	0.22	BALT2	Th/Pb	This Study
Monazite (core)	7.71	0.40	BALT4	Th/Pb	This Study
Monazite (rim)	6.32	0.20	BALT2	Th/Pb	This Study
Monazite (rim)	6.25	0.60	BALT4	Th/Pb	This Study
Adular (core)	<13.0	0.1	S1036	K/Ar	*Soom* [1986]
Adular (rim)	<10.5	0.1	S1036	K/Ar	*Soom* [1986]
White mica (mylonite)	13.7	0.1	MC420	Ar/Ar	*Campani et al*. [2010]
White mica (mylonite)	11.0	0.1	MC423	Ar/Ar	*Campani et al*. [2010]
Stage 1 (biotite)	21.1	0.2	Aa0365	Ar/Ar	*Rolland et al*. [2009]
Stage 2 (white mica, multiple samples)	13.8–12.2		-	Ar/Ar	*Rolland et al*. [2009]

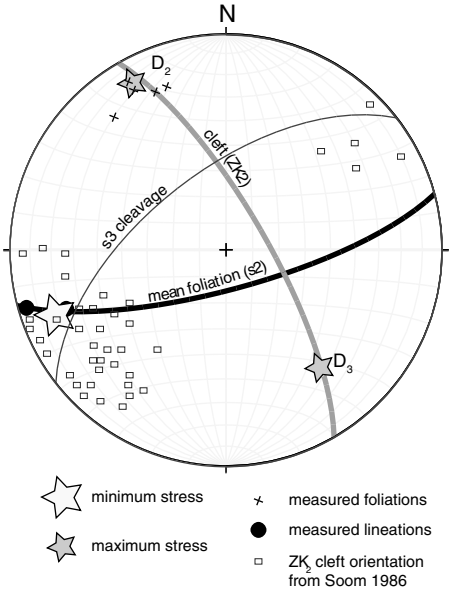

Figure 10. Orientation data and stress estimates during cleft formation in stereographic projection (Schmidt net; lower hemisphere).

relative age constraints of the clefts are consistent with its formation during the late stages of the main deformation phases (D_2/D_3; dextral transpressional deformation).

Appendix A

A1. Analytical Methods

[37] The accessory phases were systematically characterized using backscattered electron (BSE) imaging on an electron microprobe. The identified REE minerals and Y-Nb-bearing phases were analyzed on a JEOL JXA8200 electron microprobe (EMP) at the Department of Geography and Geology, University of Copenhagen. The setup for the REE minerals follows *Scherrer et al*. [2000] with modifications noted in *Janots et al*. [2008]. We measured *Kα* lines of Si, Ca, P, and *Lα* lines of As, Y, Ce, La *Lβ* lines of Pr, Dy, Sm, Ho, and *Mα* lines for Th and *Mβ* of U. In a special setup, age information is obtained by including the *M*β line for Pb. In Y-Nb-Ti oxides, additionally Nb and Ta have been measured using the *Lα* lines. We used natural and synthetic glasses and minerals as standards. The measurements were performed at 15 kV and 20 nA with counting times of 20 to 60s, depending on estimated element concentrations. For chemical dating, Pb was counted for 240 s. X-ray maps in wave dispersive mode were obtained at conditions of 15 kV, 50 nA, and counting times of 200 ms per pixel. Micas were measured with a setup measuring Si, Ti, Al, Fe, Mg, Mn, Ca, Na, and K using the *Kα* lines and 15 kV and 10 nA as operating conditions. The $\phi(\rho Z)$ matrix correction was applied to all analyses. Peak overlap was tested by using Virtual WDS [*Reed and Buckley*, 1996] and two overlap-free backgrounds were selected (for all elements). The detection limits are below ~100 ppm, whereas in this study analyses below 1000 ppm are not considered.

[38] U-Th-Pb isotope analyses of monazite were performed on a Cameca IMS1280 SIMS instrument at the Swedish Museum of Natural History (Nordsims facility). Analytical methods closely follow those described by *Harrison et al*. [1995] and *Kirkland et al*. [2009], using a -13 kV O_2^- primary beam of ca. 6 nA and nominal 15 µm diameter. The mass spectrometer was operated at +10 kV and a mass resolution of ca. 4300 (M/*Δ*M, at 10% peak height) with data collected in peak hopping mode using an ion-counting electron multiplier. U-Pb and Th-Pb data were calibrated against an in-house reference monazite, C83-32 (kindly provided by F. Corfu). Analytical details and correction procedures closely follow those described in *Kirkland et al*. [2009] and *Janots et al*. [2012]. Pb isotope signals were corrected for common Pb contribution using measured ^{204}Pb and an assumed present day Pb isotope composition predicted by the model of *Stacey and Kramers* [1975]. In monazite, ^{204}Pb is affected by an unresolvable molecular interference from doubly charged $^{232}Th^{144}Nd^{16}O_2^{++}$ (^{206}Pb and ^{207}Pb are also affected to a smaller degree by $ThNdO_2^{++}$ species), which can result in an overestimate of the amount of common Pb. The extent of this interference was monitored using $^{232}Th^{143}Nd^{16}O_2^{++}$ at mass 203.5 and a correction applied whenever the count rate exceeded the average background count on the ion-counting detector by three times its standard deviation. Whole rock major element analyses were performed at AcmeLabs using ICP-emission spectroscopy. Trace elements were analyzed by solution ICP-MS at AcmeLabs (Canada).

A2. Characterization of the Starting Material

[39] All samples show very similar bulk rock chemistry. Therefore, data may thus be used for discrimination diagrams. The bulk chemistry shows a granite with high molar $Al_2O_3/CaO+Na_2O+K_2O$ value (<1.25; Figure S1 in the supporting information). The peraluminous character is also indicated by normative corundum in this metagranitoid (CIPW norm). In addition, the different trace element diagrams plot as syncollisional granites in tectonic discrimination diagrams (Figure S1 in the supporting information) [*Pearce et al*., 1984].

[40] **Acknowledgments.** The NORDSIMS ion microprobe facility is operated by the research funding agencies of Denmark, Iceland, Norway, and Sweden, the Geological Survey of Finland and the Swedish Museum of Natural History. We thank P. Bähler for providing information on the cleft. C. Schnyder for help with sampling and Y. Rolland and B. Hacker for constructive and helpful reviews.

References

Baer, A. (1959), L'extrème occidentale du massif de l'Aar, *Bull. Soc. Neuchâtel Sci. Nat.*, *82*, 1–160.

Bernet, M. (2009), A field-based estimate of the zircon fission-track closure temperature, *Chem. Geol.*, *259*, 181–189.

Bousquet, R., et al. (2012), Metamorphic framework of the Alps, Map of CCGM/CGMW.

Campani, M., N. Mancktelow, D. Seward, Y. Rolland, W. Müller, and I. Guerra (2010), Geochronological evidence for continuous exhumation through the ductile-brittle transition along a crustal scale low-angle normal fault: Simplon Fault Zone, central Alps, *Tectonics*, *29*, TC3002, doi:10.1029/2009TC002582.

Dolivo, E. (1982), Nouvelles observations structurales au SW du massif de l'Aar entre Visp et Gampel, *Beitr. Geolog. Karte Schweiz (N.F.)*, *157*, 1–82.

Ewing, R., W. J. Weber, and F. W. Clinard Jr. (1995), Radiation effects in nuclear waste forms for high-level radioactive waste, *Progr. Nucl. Energy*, *29*, 63–127.

Fellenberg, E. (1893), Geologische beschreibung des westlichen theils des Aarmassivs, enthalten auf dem nördlich der Rhone gelegen theile des blattes XVIII der Dufour-karte, *Beitr. Geol. Karte Schweiz*, *23*, 1–83.

Frey, M., and B. Wieland (1975), Chloritoid in autochthon-parautochthonen sedimenten des Aarmassivs, *Schweiz. Mineral. Petrogr. Mitt.*, *55*, 407–418.

Frey, M., J. Desmons, and F. Neubauer (1999), The new metamorphic map of the Alps: Introduction, *Schweiz. Mineral. Petrogr. Mitt.*, *79*, 1–4.

Gasquet, D., J.-M. Bertrand, J.-L. Paquette, J. Lehmann, G. Ratzov, R. D. A. Guedes, M. Tiepolo, A.-M. Boullier, S. Scaillet, and S. Nomade (2010), Miocene to Messinian deformation and hydrothermal activity in a pre-Alpine basement massif of the French western Alps: New U–Th–Pb and argon ages from the Lauzière massif, *Bull. Soc. Géol. France*, *181*, 227–241.

Gasser, U., and E. Dolivo (1980), Nouvelles observations sur la géologie du Heidnischbiel (Raron, VS), *Bull. Soc. Vaud Sci. Nat.*, *75*, 9–22.

Giudotti, C. V. (1984), Micas in metamorphic rocks, in *Micas, Rev. in Mineral.*, vol. 13, edited by S. W. Bayley, pp. 357–467, Mineral. Soc. of Am., Washington, D. C.

Harrison, T. M., K. D. McKeegan, and P. LeFort (1995), Detection of inherited monazite in the Manaslu leucogranite by ion microprobe dating: crystallization age and tectonicimplications, *Earth Planet. Sci. Lett.*, *133*, 271–282.

Janots, E., M. Engi, A. Berger, J. Allaz, J. O. Schwarz, and C. Spandler (2008), Prograde metamorphic sequence of REE minerals in pelitic rocks of the Central Alps, implications for allanite–monazite–xenotime phase relations from 250 to 610 °C, *J. Metam. Geol.*, *26*, 509–526.

Janots, E., A. Berger, E. Gnos, M. Whitehouse, E. Lewin, and T. Pettke (2012), Constraints on fluid evolution during metamorphism from U–Th–Pb systematics in Alpine hydrothermal monazite, *Chem. Geol.*, *326–327*, 61–71.

Kirkland, C. L., M. J. Whitehouse, and T. Slagstad (2009), Fluid-assisted zircon and monazite growth within a shear zone: A case study from Finnmark, Arctic Norway, *Contrib. Mineral. Petrol.*, *158*, 637–657.

Labhardt, T. P. (1965), Petrotektonische untersuchungen am südrand des Aarmassivs Nördlich Naters (Wallis, Schweiz), *Beitr. Geolog. Karte Schweiz (N.F.)*, *124*, 1–81.

Mannucci, G., V. Diella, C. M. Gramaccioli, and T. Pilati (1986), A comparative study of some pegmatitic and fissure monazite from the Alps, *Can. Mineral.*, *24*, 469–474.

Michalski, I., and M. A. Soom (1990), The Alpine thermo-tectonic evolution of the Aar and Gotthard massifs, central Switzerland: Fission track ages on zircon and apatite and K/Ar mica ages, *Schweiz. Mineral. Petrogr. Mitt.*, *70*, 373–387.

Mullis, J., J. Dubessy, B. Poty, and J. O'Neil (1994), Fluid regimes during late stages of a continental collision: Physical, chemical, and stable-isotope measurements of fluid inclusions in fissure quartz from a geotraverse through the Central Alps, Switzerland, *Geochim. Cosmochim. Acta*, *58*, 2239–2267.

Niggli, P., J. G. Königsberger, and R. L. Parker (1940), *Die Mineralien der Schweizeralpen*, B. Wepf, Basel.

Pearce, J. A., N. B. W. Harris, and A. G. Tindle (1984), Trace element discrimination diagrams for the tectonic interpretation of granitic rocks, *J. Petrol.*, *25*, 956–983.

Pleuger, J., N. Mancktelow, H. Zwingmann, and M. Manser (2012), K–Ar dating of synkinematic clay gouges from Neoalpine faults of the Central, Western and Eastern Alps, *Tectonophysics*, *550–553*, 1–16, doi:10.1016/j.tecto.2012.05.001.

Poty, B., H. Stalder, and A. M. Weisbrod (1974), Fluid inclusions studies in quartz from fissures of Western and Central Alps, *Schweiz. Mineral. Petrogr. Mitt.*, *54*, 717–752.

Reed, S. J. B., and A. Buckley (1996), Virtual WDS, *Microchim. Acta*, *13*, 479–483.

Regis, D., B. Cenki-Tok, J. Darling, and M. Engi (2012), Redistribution of REE, Y, Th, and U at high pressure: Allanite-forming reactions in impure meta-quartzites (Sesia Zone, Western Italian Alps), *Am. Mineral.*, *97*, 315–328.

Reinecker, J. M. Danisik, C. Schmid, C. Glotzbach, M. Rahn, W. Frisch, and C. Spiegel (2008), Tectonic control on the late stage exhumation of the Aar Massif (Switzerland): Constraints from apatite fission track and (U-Th)/He data, *Tectonics*, *27*, TC6009, doi:10.1029/2007TC002247.

Rolland, Y., S. F. Cox, A.-M. Boullier, G. Pennacchioni, and N. Mancktelow (2003), Rare earth and trace element mobility in mid-crustal shear zones: Insights from the Mont Blanc Massif (Western Alps), *Earth Planet. Sci. Lett.*, *214*, 203–219.

Rolland, Y., M. Rossi, S. F. Cox, M. Corsini, N. Mancktelow, G. Pennacchioni, M. Fornari, A. M. Boullier (2008), $^{40}Ar/^{39}Ar$ dating of synkinematic white mica: Insights from fluid-rock reaction in low-grade shear zones (Mont Blanc Massif) and constraints on timing of deformation in the NW External Alps, in *The Internal Structure of Fault Zones: Implications for Mechanical and Fluid-Flow Properties*, edited by C. A. J. Wibberley et al., *Geolog. Soc. London Spec. Publ.* vol. 299, 293–315, doi:10.1144/SP299.17.

Rolland, Y., S. F. Cox, and M. Corsini (2009), Constraining deformation stages in brittle-ductile shear zones from combined field mapping and $^{40}Ar/^{39}Ar$ dating: The structural evolution of the Grimsel Pass area (Aar Massif, Swiss Alps), *J. Struct. Geol.*, *31*, 1377–1394.

Sanchez, G., Y. Rolland, M. Corsini, E. Oliot, P. Goncalves, J. Schneider, C. Verati, J. M. Lardeaux, and D. Marquer (2011), Dating low-temperature deformation by $^{40}Ar/^{39}Ar$ on white mica, insights from the Argentera-Mercantour Massif (SW Alps), *Lithos*, *125*, 521–536.

Schaltegger, U. (1994), Unraveling the pre-Mesozoic history of Aar and Gotthard Massifs (Central Alps) by isotopic dating – a review, *Schweiz. Mineral. Petrogr. Mitt.*, *74*, 41–51.

Schenker, M. (1946), Geologische untersuchungen der Mesozoischen sedimentkeil am südrand des Aarmassivs zwischen Lonza und Baltschiedertal (Wallis), *Beitr. Geolog. Karte Schweiz (N.F.)*, *86*, 1–60.

Scherrer, N. C., M. Engi, E. Gnos, V. Jakob, and A. Liechti (2000), Monazite analysis: From sample preparation to microprobe age dating and REE quantification, *Schweiz. Mineral. Petrogr. Mitt.*, *80*, 93–105.

Sharp, Z. D., H. Masson, and R. Lucchini (2005), Stable isotope geochemistry and formation mechanisms of quartz veins; extreme paleoaltitudes of the Central Alps in the Neogene, *Am. J. Sci.*, *305*, 187–219.

Soom, M. (1986), Geologie und petrographie von Ausserberg (VS). Kluftmineralisation am Südrand des Aarmassivs, 129 pp., Lizenziat-Arbeit Univ. Bern, Bern.

Stacey, J. S., and J. D. Kramers (1975), Approximation of terrestrial lead isotope evolution by a two-stage model, *Earth Planet. Sci. Lett.*, *26*, 207–221.

Stalder, H. A. (1990), Erdwissenschaftliche Abteilung (bericht über mineraleingänge im museum), *Jb. Naturhist. Mus. Bern*, *10*, 29–48.

Steck, A. (1966), Petrographische untersuchungen am Zentralen Aaregranit und Seinen altkristallinen Hüllgesteinen im westlichen Aarmassiv im gebiet Belalp-Grisighorn, *Beitr. Geol. Karte Schweiz (N.F.)*, *130*, 1–99.

Steck, A. (1968), Die alpidischen strukturen in den Zentralen Aaregraniten des westlichen Aarmassivs, *Eclogae Geol. Helv.*, *61*, 19–48.

Stipp, S. L. S., J. T. Christensen, L. Z. Lakshtanov, J. Baker, and T. E. Waight (2006), Rare Earth element (REE) incorporation in natural calcite: A model for actinide uptake in a secondary phase, *Radiochim. Acta*, *94*, 523–528.

Tarantola, A., J. Mullis, T. Vennemann, J. Dubessy and C. DeCapitani (2007), Oxidation of methane at the CH_4/H_2O-(CO_2) transition zone in the external part of the Central Alps, Switzerland: Evidence from stable isotope investigation, *Chem. Geol.*, *237*, 329–357.

Yamada, R., T. Tagami, S. Nishimura, and H. Ito (1995), Annealing kinetics of fission tracks in zircon: An experimental study, *Chem. Geol.*, *122*, 249–258.